

Numerical modeling and dynamic analysis of the 2017 Xinmo landslide in Maoxian County, China

OUYANG Chao-jun^{1,2}  <http://orcid.org/0000-0001-9972-4698>; e-mail: cjouyang@imde.ac.cn

ZHAO Wei^{1,2}  <http://orcid.org/0000-0003-1883-0566>; e-mail: 358250481@qq.com

HE Si-ming^{1,2,3}  <http://ORCID.org/0000-0002-9074-9298>; e-mail: hsm@imde.ac.cn

WANG Dong-po^{1,4}  <http://orcid.org/0000-0002-6172-4753>; e-mail: dongpo_007@163.com

ZHOU Shu^{1,2*}  <http://orcid.org/0000-0002-7904-4748>;  e-mail: zhoushucsu@163.com

AN Hui-cong^{1,2}  <http://orcid.org/0000-0003-0609-7096>; e-mail: m18811380306@163.com

WANG Zhong-wen⁴  <http://orcid.org/0000-0003-1885-0014>; e-mail: 534667665@qq.com

CHENG Duo-xiang⁵  <http://orcid.org/0000-0003-4648-9158>; e-mail: 270932765@qq.com

* Corresponding author

1 Key laboratory of Mountain Hazards and Surface Process & Institute of Mountain Hazards and Environment (IMHE), Chinese Academy of Sciences, Chengdu 610041, China

2 University of Chinese Academy of Sciences, Beijing 100049, China

3 Center for Excellence in Tibetan Plateau Earth Sciences, Chinese Academy of Sciences, Beijing 100101, China

4 State Key Laboratory of Geohazard Prevention and Geoenvironment Protection, Chengdu University of Technology, Chengdu 610059, China

5 Sichuan Engineering Research Center for Emergency Mapping & Disaster Reduction/Sichuan Geomatics Center, Chengdu 610041, China

Citation: Ouyang CJ, Zhao W, He SM, et al. (2017) Numerical modeling and dynamic analysis of the 2017 Xinmo landslide in Maoxian County, China. Journal of Mountain Science 14(9). <https://doi.org/10.1007/s11629-017-4613-7>

© Science Press and Institute of Mountain Hazards and Environment, CAS and Springer-Verlag GmbH Germany 2017

Abstract: A catastrophic landslide occurred at Xinmo village in Maoxian County, Sichuan Province, China, on June 24, 2017. A 2.87×10^6 m³ rock mass collapsed and entrained the surface soil layer along the landslide path. Eighty-three people were killed or went missing and more than 103 houses were destroyed. In this paper, the geological conditions of the landslide are analyzed via field investigation and high-resolution imagery. The dynamic process and runout characteristics of the landslide are numerically analyzed using a depth-integrated continuum method and MacCormack-TVD finite difference algorithm. Computational results show that the evaluated area of

the danger zone matches well with the results of field investigation. It is worth noting that soil sprayed by the high-speed blast needs to be taken into account for such kind of large high-locality landslide. The maximum velocity is about 55 m/s, which is consistent with most cases. In addition, the potential danger zone of an unstable block is evaluated. The potential risk area evaluated by the efficient depth-integrated continuum method could play a significant role in disaster prevention and secondary hazard avoidance during rescue operations.

Keywords: Xinmo landslide; Runout; Numerical modeling; Dynamic process; Potential risk; High-locality landslide

Received: 26 July 2017

Revised: 20 August 2017

Accepted: 23 August 2017

Introduction

People living in mountainous areas commonly face tremendous threats from landslides or rock falls. A variety of factors impose restrictions on moving personnel out of dangerous areas. At about 5:39 AM on June 24, 2017, a catastrophic landslide occurred at Xinmo village ($E 103^{\circ}39' 03''$, $N 32^{\circ}04' 09''$), Maoxian County, Sichuan province, China. The beautiful village, a famous scenic spot, was completely buried by rushing high-speed rock and soil aggregates, and Eighty-three people were killed or went missing and more than 103 houses were destroyed. The location of the landslide is very close to the epicenter of the Diexi Ms 7.5 earthquake in 1933. Many bead-like barrier dams and old landslides could be easily discriminated in the area. The initial collapse of this landslide occurred at an elevation of about 3800 m above sea level. The high altitude makes on-foot investigation difficult. In addition, it is hard to obtain high-quality remote sensing information about land surface deformation due to the thick forest in the area. Thus, analysis of the failure mechanism and dynamic characteristics of landslides with high potential energy is difficult (Guthrie et al. 2009; Xu et al. 2010; Burgh et al. 2012; Wu et al. 2013; Coe et al. 2016; Wang et al. 2017).

After the disaster, scientists arrived on the scene and collected a variety of data, such as high-resolution images, pre- and post-landslide elevation, land surface deformation, seismic, InSAR, and Radar data. Such comprehensive work can be expected to provide significant guidance to similar cases in the future to prevent casualties and protect property.

Numerical analysis of landslide propagation and the danger area is significantly important for risk evaluation before a landslide and during the rescue stage. Numerical modeling techniques including the discrete element method (Banton et al. 2009; Zhou et al. 2013; Shi et al. 2016), discontinuous deformation analysis (DDA) (Zhang et al. 2016; Beyabanaki et al. 2016) and depth-integrated continuum mechanics method (Iverson et al. 2015; Ouyang et al. 2017), have been continuously shown to successfully reproduce the dynamic process of rockslides. Among the above-mentioned methods, the depth-integrated continuum model, which greatly reduces

computation time (Iverson and Ouyang 2015), has been broadly and successfully applied in modeling of earth-surface flows, such as landslides (Iverson and George 2015; Ouyang et al. 2017), debris flows (Ouyang et al. 2015a; Chen et al. 2016), hydrodynamic flows (Liang 2010; Ouyang et al. 2015b), rock or snow avalanches (Delaney and Evans 2015), multi-phase flows (He et al. 2016), and landslides into rivers (Liu et al. 2016). The depth-integrated continuum method simplifies the classical Navier-Stokes model by considering the main characteristics of gravity-driven surface flows. Thus, it requires far fewer parameters and is solved much more efficiently. It is believed to become a significant tool for pre-evaluating risk areas and guiding mitigation design in the near future.

In this paper, the landslide at Xinmo village on June 24, 2017 in Maoxian County (hereafter called Xinmo landslide), China is analyzed in detail. Firstly, the geological conditions, causes, and mechanisms of the landslide are introduced. Secondly, the depth-integrated continuum framework and MacCormack-TVD finite difference algorithm, which has second-order accuracy in both time and space, are introduced. Thirdly, numerical modeling of the landslide propagation is performed and compared with field observations. Fourthly, the potential danger area of a determined unstable block is evaluated.

1 Background

1.1 Geological conditions and properties

For Xinmo landslide, the initial failure block is located at $E 103^{\circ}39' 03''$, $N 32^{\circ}04' 09''$. The general features of the landslide are shown in Figure 1. The location lies at the left bank of the V-shaped Songping gully, which is the first tributary of the Minjiang river. The area is located in an active earthquake zone and belongs to Longmenshan tectonic belt. Strong earthquakes such as the Ms 7.5 Diexi earthquake in 1933, Ms 7.2 Songpan earthquake in 1976 and Ms 8.0 Wenchuan earthquake in 2008 have greatly affected the rock masses.

According to data from Sichuan meteorological bureau, the study area has a mean annual precipitation of 484.1 mm, and the maximum

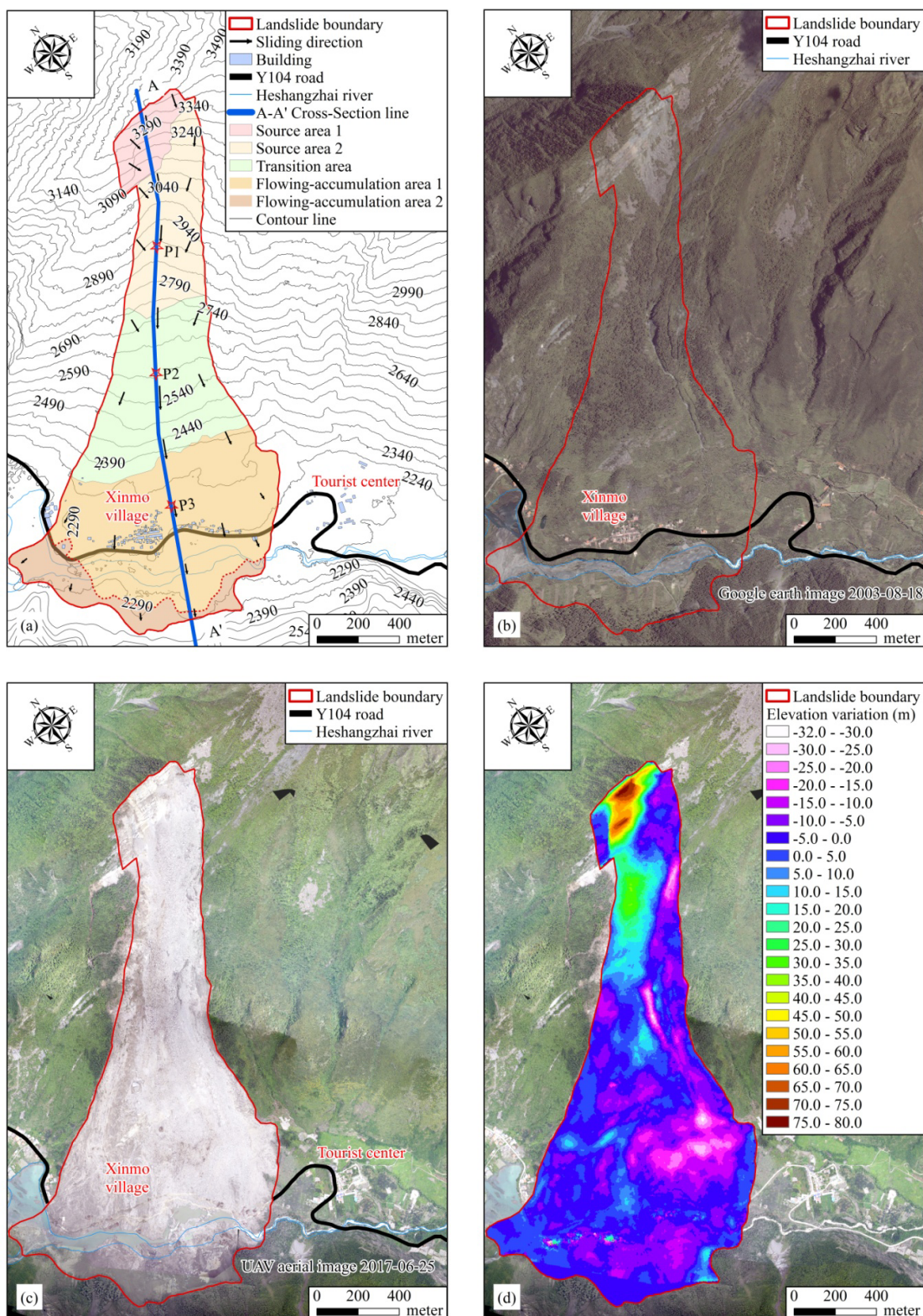


Figure 1 Features of the Xinmo landslide (a) The topographic map of the landslide; (b) Google earth image taken in 2003; (c) An overview of the post-landslide at Xinmo village (image taken by UAV on June 25, 2017); (d) The elevation variations estimated on the pre-and pos-failure DEMs; (e) The unstable block determined by images and field investigation. (-to be continued-)

(-Continued-)

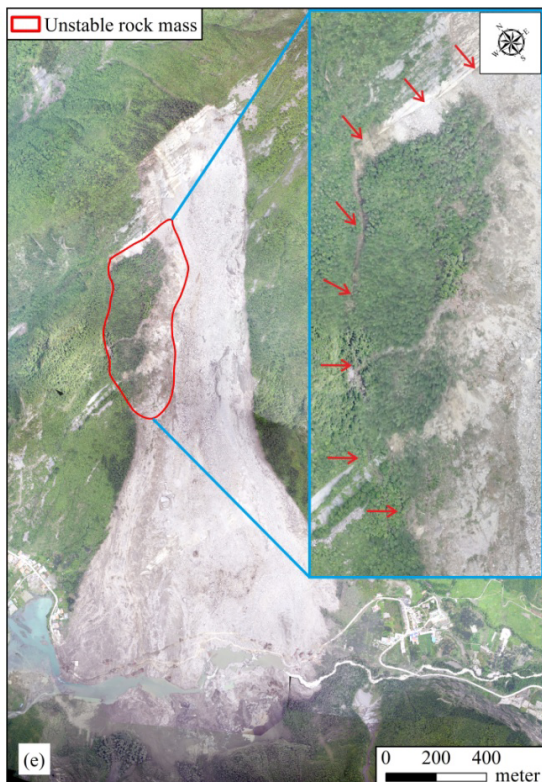


Figure 1 Features of the Xinmo landslide (a) The topographic map of the landslide; (b) Google image earth taken in 2003; (c) An overview of the post-landslide at Xinmo village (image taken by UAV on June 25,2017); (d) The elevation variations estimated on the pre-and pos-failure DEMs; (e) The unstable block determined by images and field investigation.

annual rainfall is 560.6 mm. The maximum rainfall in single day is 75.2 mm. Rainfall is concentrated from April to October. In that period, total rainfall is about 444.4 mm, which accounts for 91.8% of the annual precipitation. In 2017, the cumulative rainfall between May 1 and June 22 was 201 mm at Diexi town and 227 mm at Songping gully. There was continuous rainfall for 10 to 20 days before the landslide failure (Figure 2).

1.2 Dynamic process and runout characteristics

High-resolution images and terrain elevation data before and after landslide were provided by the Sichuan Geomatics Center (Figure 1(a)-(d)). The geometric feature analysis can be referred to Fan et al (2017). Based on the images and field investigation, the initial failure, dynamic

propagation and deposition characteristics are analyzed in detail. The altitude of the rear of the landslide is about 3400m, and the slope toe is about 2150 m. The mobility of this landslide was evaluated as about 0.42 by the expert group within this investigation team.

The landslide can be generally divided into three areas, source, transition, and flowing-accumulation as shown in Figure 1(a). The source area consists of two parts. Source area 1 contains the initial collapsed rock mass and has a volume of 2.87×10^6 m³. Source area 2 is the superficial mass below source area 1, which was rapidly entrained by the strong impact of the slide. The total volume of the two parts is 5.08×10^6 m³. The transition area is bound by light green color in Figure 1(a). The flow-accumulation area contains the terrace and river bank, where houses were built. The maximum depth of the deposited mass is more than 32 m. Most houses in the terrace were totally buried and destroyed. It is worth noting that large quantities of sprayed soil were found in the landslide front due to high-speed blasting. The depth of the sprayed soil is less than 3m and the range of this area is marked as flowing-accumulation area 2 by the red dotted line, as shown in Figure 1(a). The triggering mechanism with detail can be referred to Su et al (2017).

During rescue operations, it was noticed that huge deformed unstable masses with a volume of 3.03×10^6 m³ are dangerously prone to collapse. A rupture tens meters wide in the free face indicates that this rock mass is a high-risk source. The potential danger range is analyzed in section 3.3.

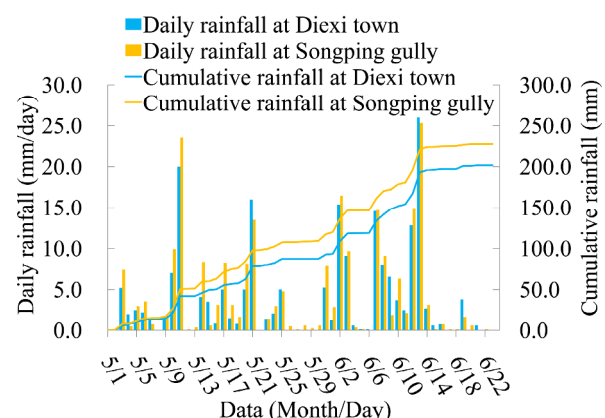


Figure 2 Daily rainfall (column charts) and cumulative rainfall (line charts) from May 1, 2017 to June 22, 2017.

2 Model Description and Solution

2.1 Depth-integrated continuum method

For the Maoxian landslide, the dynamic process and runout characteristics are analyzed using a depth-integrated continuum method. In a depth-integrated continuum framework, the mass and momentum equations in rectangular Cartesian coordinates with a vertical z-axis can be derived as

$$\frac{\partial(h)}{\partial t} + \frac{\partial(h\bar{u})}{\partial x} + \frac{\partial(h\bar{v})}{\partial y} = 0 \quad (1)$$

$$\frac{\partial(h\bar{u})}{\partial t} + \frac{\partial(h\bar{u}^2 + k_x gh^2 / 2)}{\partial x} + \frac{\partial(h\bar{u}\bar{v})}{\partial y} = k_x gh \frac{\partial z_b}{\partial x} - \frac{(\tau_{zx})_b}{\rho} \quad (2)$$

$$\frac{\partial(h\bar{v})}{\partial t} + \frac{\partial(h\bar{u}\bar{v})}{\partial x} + \frac{\partial(h\bar{v}^2 + k_y gh^2 / 2)}{\partial y} = k_y gh \frac{\partial z_b}{\partial y} - \frac{(\tau_{zy})_b}{\rho} \quad (3)$$

where ρ represents flow density; h is flow height; u and v are depth-integrated flow velocity in x and y direction; $(\tau_{zx})_b$ and $(\tau_{zy})_b$ are basal resistance components; k_x and k_y are lateral earth pressure coefficients which are given by

$$k_x = \begin{cases} k_{active} & (\partial\bar{u}/\partial x > \epsilon) \\ 1 & (|\partial\bar{u}/\partial x| \leq \epsilon) \\ k_{passive} & (\partial\bar{u}/\partial x < -\epsilon) \end{cases} \quad (4)$$

$$k_y = \begin{cases} k_{active} & (\partial\bar{v}/\partial y > \epsilon) \\ 1 & (|\partial\bar{v}/\partial y| \leq \epsilon) \\ k_{passive} & (\partial\bar{v}/\partial y < -\epsilon) \end{cases} \quad (5)$$

where ϵ is small and used as a threshold to avoid the machine precision error. The lateral earth pressure coefficients in the active elongation (k_{active}) and passive compression ($k_{passive}$) depend on the strain rate of the moving material columns, as suggested by Savage and Hutter (Savage and Hutter 1989);

$$\left. \begin{array}{l} k_{active} \\ k_{passive} \end{array} \right\} = \frac{2}{\cos^2 \phi} \times \left[1 \mp \sqrt{1 - (1 + \tan^2 \delta) \cos^2 \phi} \right] - 1 \quad (6)$$

where ϕ and δ are the internal and bed friction angles.

The basal friction stress τ_b is assumed to obey

the following Coulomb failure criterion

$$\tau_b = c + \bar{\rho}gh \tan(\delta) \quad (7)$$

c and δ are the cohesion and basal friction angle of the mass.

The depth-integrated mass and momentum equations (1-3) are solved by Massflow, which is a high-efficiency finite difference framework based on a MacCormack-TVD scheme (Ouyang et al. 2013; 2015a, b; 2017). A variable timestep is adopted and guaranteed by a Courant number. The computational codes are optimized and sped up by using Fortran programming and parallel computing. Its robustness has been verified by a series of experimental benchmarks and real hazards (Ouyang et al. 2015a, b; Ouyang et al. 2017).

3 Numerical Analysis of the Landslide Dynamic Propagation

3.1 Computational setup

The pre-landslide topography with a precision of 5 m was provided by Sichuan Geomatics Center. One day after the incident, high-performance UAV aerial photogrammetry was performed by the Sichuan Geomatics Center and high-resolution elevation with 0.5 m precision was created. The landslide range was determined from images and verified by field investigation. In the computation, the initial source consists of the collapsed rock mass and the triggered surface soil layer. The precise volume is determined by the terrain difference before and after landslide. In order to consider the volume amplification due to masses disintegration, the initial source is enlarged to 1.4, which is consistent with similar rockslides (Hung and Evans 2004; Xing et al. 2014).

3.2 Analysis of computational results

The Coulomb basal frictional model as expressed in Eq. (7) was adopted. The mobility of this landslide, which is indicated by the ratio (H/L) of flow height H to length L was evaluated as 0.42 by an expert group within this investigation team. Thus, the coefficient of basal friction angle was adopted as 0.42. A cohesion of 20 kpa was adopted.

It is useful to describe the accumulation behavior in the static stage. Lateral earth pressure was considered and the internal friction angle was set as 35° , which is reasonable and somewhat larger than the friction angle for soil material (Ouyang et al. 2017). In order to take volume bulking into account, the volume was amplified 40% in the initial stage. The computational cell size is set as 5 m and a variable timestep based on Courant rule is chosen for all cases.

The contours of mass depth of the Maoxian landslide at times $t = 0, 10, 20, 40, 60, 100$ seconds are shown in Figure 3. The initial collapsed rock masses rushed down and propagated fast in the direction of S 205.9° W. It quickly merged with the triggered surface soil layer. Thus, in the computation, the source area containing the two parts is considered. When $t = 10$ s, the front of landslide moves to the edge of the channel and changes its direction to S 217° W. Without the blockage formed by the terrain, the tourist center in the right valley might be damaged by the slide. When $t = 40$ s, the mass reaches the smooth terrain and begins to accumulate. After 60 s, the landslide

has almost stopped and most of the mass is deposited along the hillside and valley. The main simulated depositional domain is located in the measured range enclosed by red line (Figure 3(f)). In addition, the computed deep depositional zone in Figure 3(f) is coincident with field investigation in Figure 1(d). The computed landslide front is a little shorter than the real landslide front. This could be attributed to two reasons. Reason one is that erodible material in the transition and accumulation area is neglected in the current computation. Reason Two is that soil sprayed by the high-speed blast is difficult to account for.

The landslide flow velocity contours at times $t = 10, 20, 40, 60, 100$ seconds are shown in Figure 4. In the initial stage within 0 to 10 s, the rock collapses and the front of the sliding mass reaches a velocity of 55 m/s. At $t = 20$ s, the velocity of the right side of the slide is larger than the velocity of the left side causing more material to be deposited on the right side of the slide (Figure 1d). After 40 s, most of the mass starts to decelerate due to basal friction. After 100 s, the flow velocity in most of the slide is almost static except on some steep slopes.

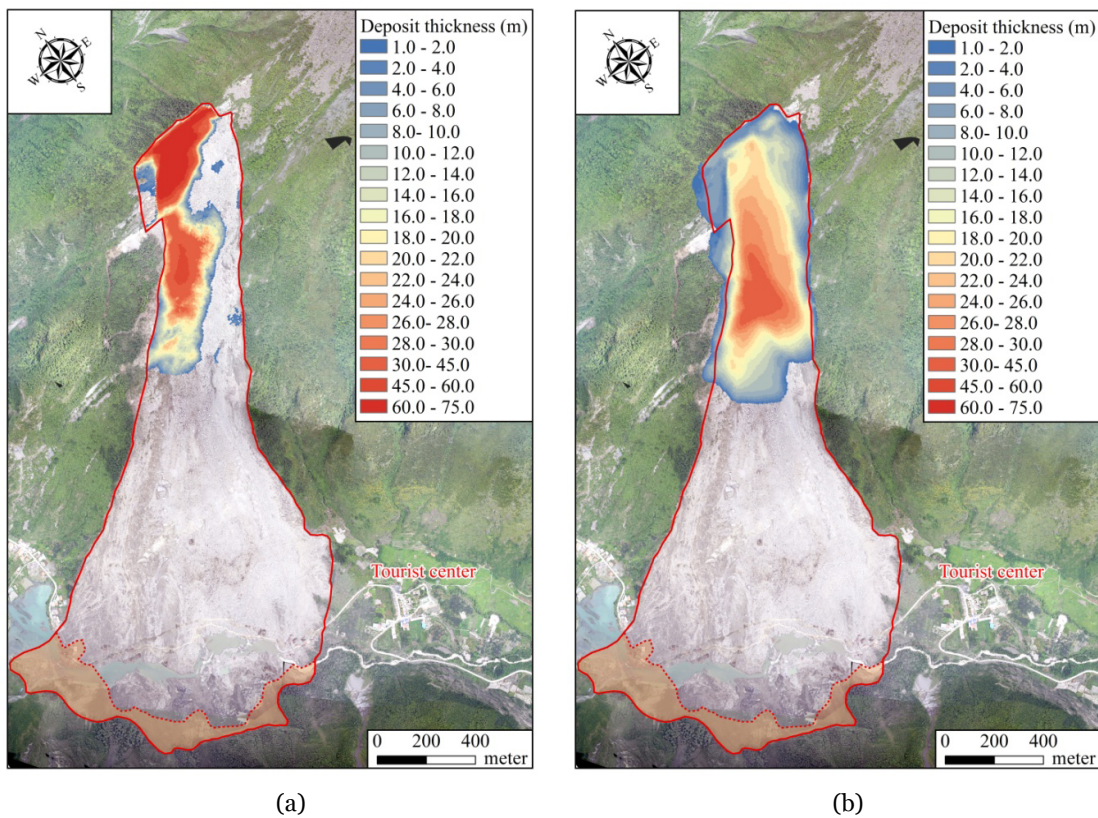


Figure 3 Snapshots of computed flow height contours of the landslide at (a) $t = 0$ s, (b) $t = 10$ s, (c) $t = 20$ s, (d) $t = 40$ s, (e) $t = 60$ s, (f) $t = 100$ s. (to be continued)

(-Continued-)

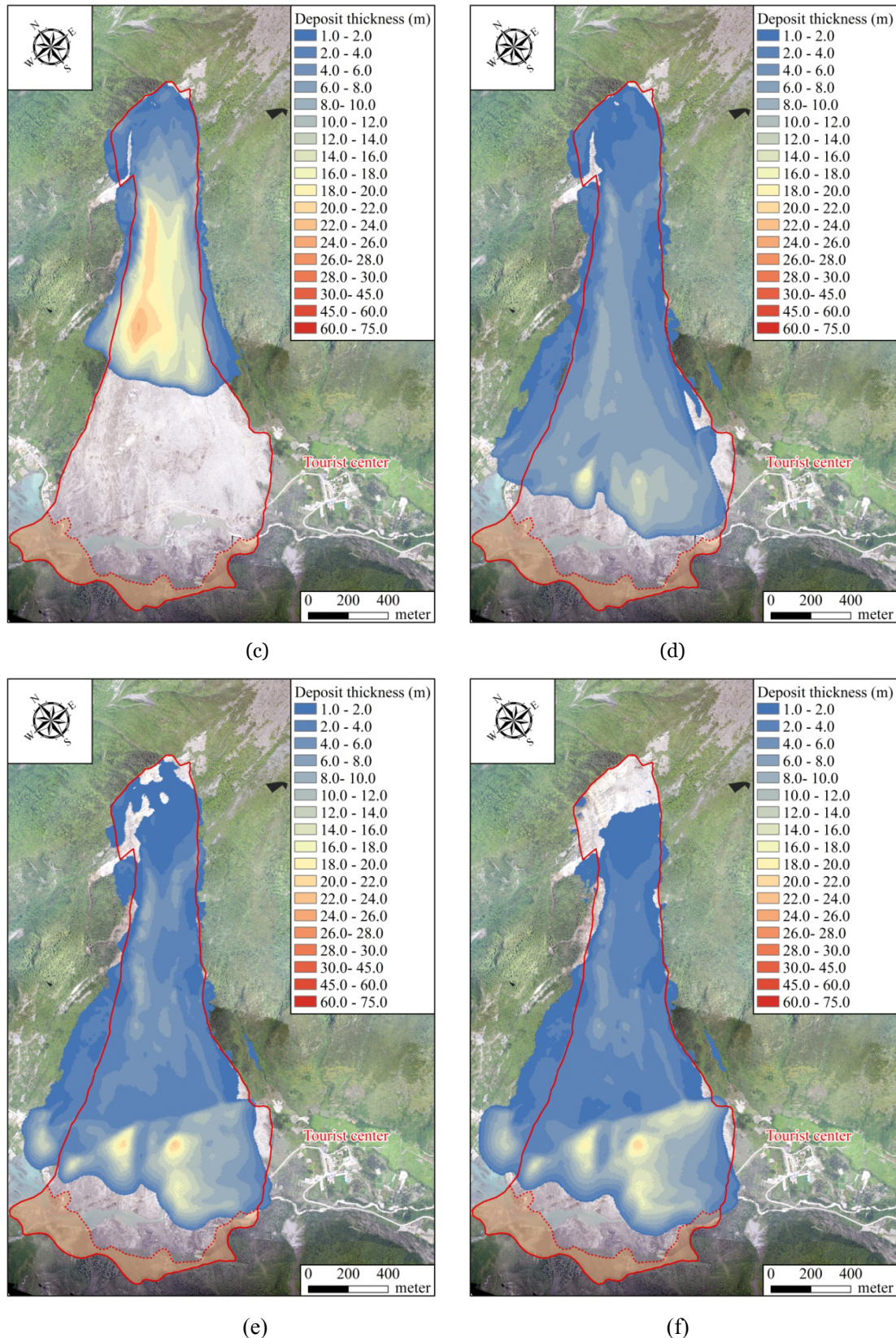


Figure 3 Snapshots of computed flow height contours of the landslide at (a) $t = 0$ s, (b) $t = 10$ s, (c) $t = 20$ s, (d) $t = 40$ s, (e) $t = 60$ s, (f) $t = 100$ s.

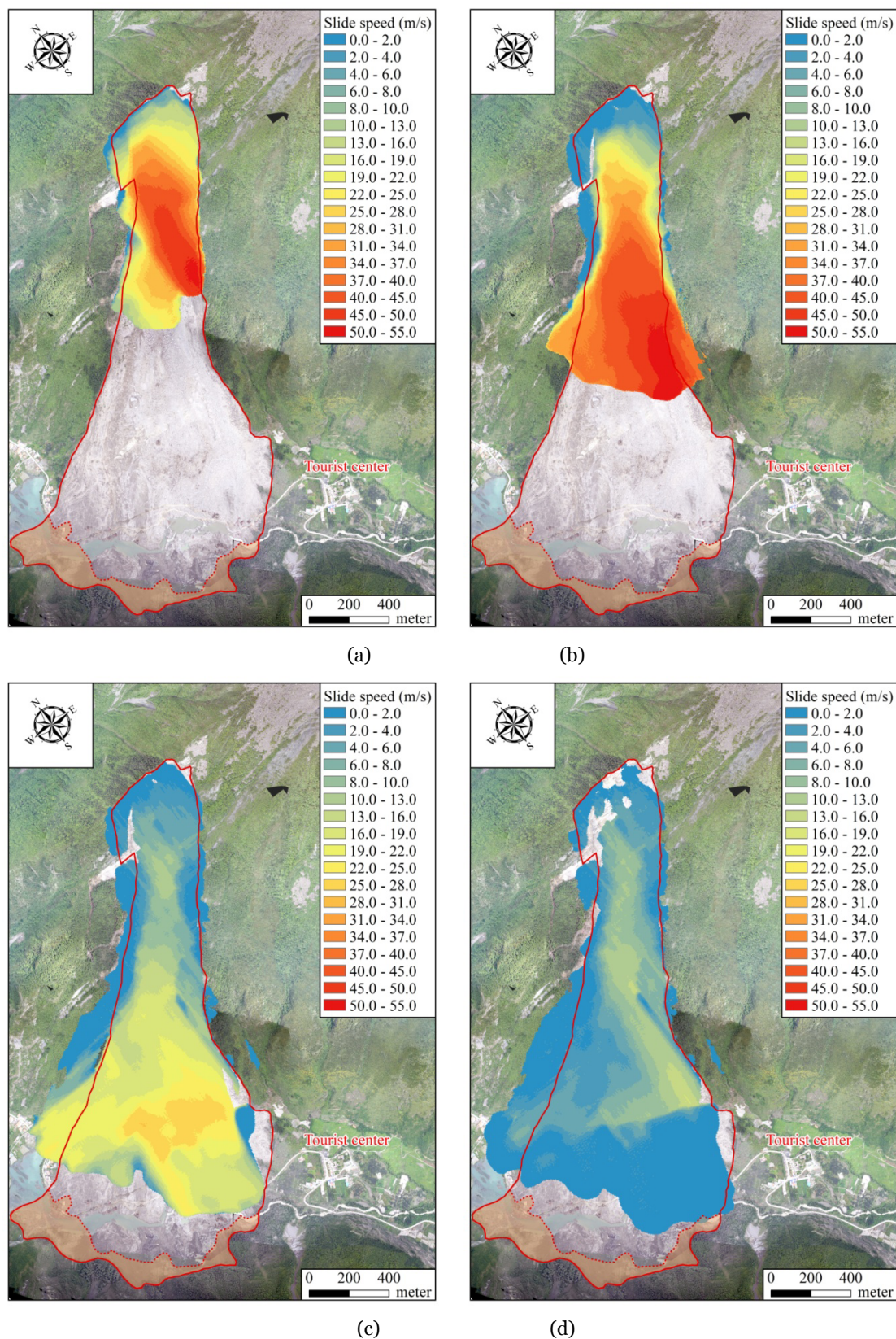
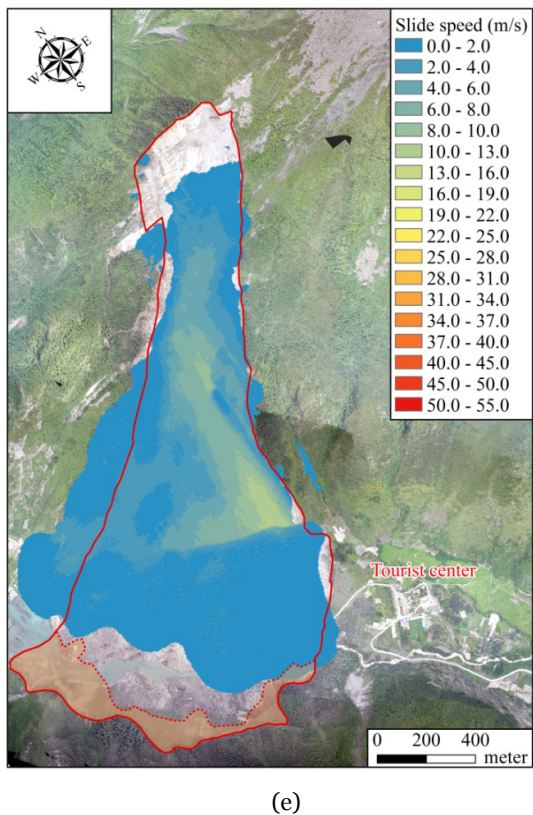


Figure 4 Snapshots of the computed flow velocity contours of the landslide at (a) $t = 10$ s, (b) $t = 20$ s, (c) $t = 40$ s, (d) $t = 60$ s, (e) $t = 100$ s. (-to be continued-)

(-Continued-)



(e)

Figure 4 Snapshots of the computed flow velocity contours of the landslide at (a) $t = 10$ s, (b) $t = 20$ s, (c) $t = 40$ s, (d) $t = 60$ s, (e) $t = 100$ s.

Velocity histories over time in three different locations of the main profile are shown in Figure 5. Locations are marked by P1–P3 in Figure 1(a). The maximum velocity for all the three locations is

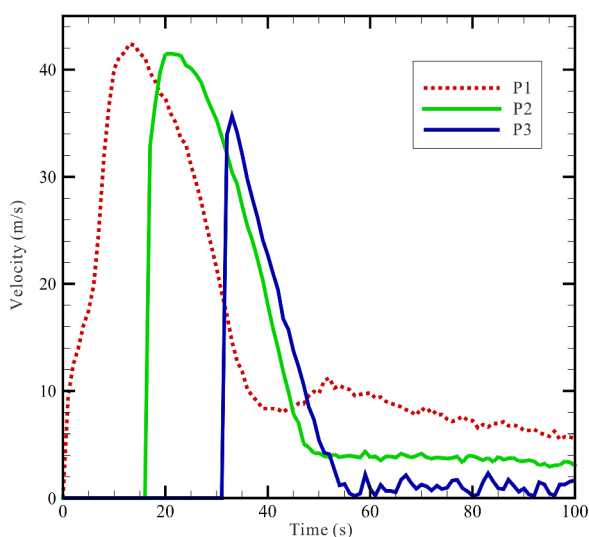


Figure 5 Velocity histories over time in three different locations P1–P3 of the main profile A-A'.

more than 35 m/s, large enough to destroy all of the simple houses and structures.

3.3 Analysis of danger areas of unstable masses

As shown in Figure 1(e), from field monitoring and high-resolution images, the unstable block is highly prone to failure. A rupture tens of meters wide can be found along the trailing edge of the landslide. A crack formed in the left edge and the whole block could collapse anytime. In order to avoid secondary hazards during rescue operations, the potential danger area of the block is evaluated by the efficient depth-integrated continuum method. According to field investigations, it is assumed that averaged initial thickness of potential failure blocks is 20 m, and initial volume is about 3.06×10^6 m³. Similarly, the initial volume is amplified by 1.4 times in the computation.

All the parameters are same as the previous analysis of the landslide dynamic process. The dynamic characteristics and predicted danger area of the unstable block is shown in Figure 6. Its motion trail is similar to the previous real landslide, and its runout is smaller than the runout of the real case. The maximum thickness of the deposited mass is 19 m and the maximum velocity is 40 m/s. Similarly, taking soil or rocks sprayed by the high-speed blast into account, the real danger area would be somewhat larger than the initial slide. Thus, the whole rescue area should be continuously monitored.

4 Conclusions

On 24 June 2017, a catastrophic landslide occurred at Xinmo village in Maoxian, Sichuan, China. The geological background and characteristics of the landslide are analyzed. The depth-integrated continuum method is adopted to numerically simulate the dynamic process of this landslide. Computational results agree well with the field investigation. The computational trajectory path and depositional range match well with data collecting in the field. The computational maximum velocity is about 55 m/s. The Coulomb model is feasible to evaluate the dynamic propagation of large landslides.

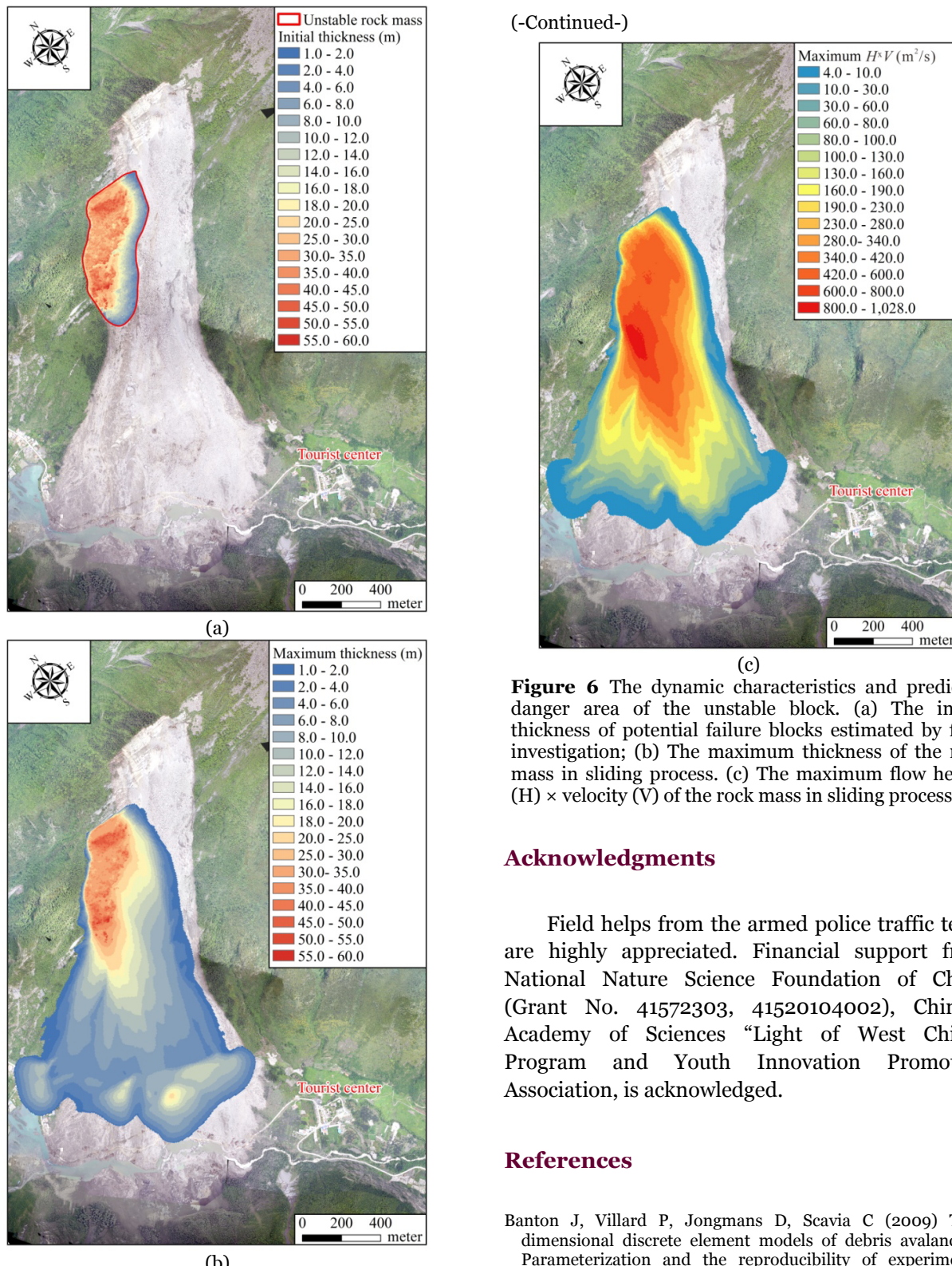


Figure 6 The dynamic characteristics and predicted danger area of the unstable block. (a) The initial thickness of potential failure blocks estimated by field investigation; (b) The maximum thickness of the rock mass in sliding process. (c) The maximum flow height (H) \times velocity (V) of the rock mass in sliding process. (- to be continued-)

(-Continued-)

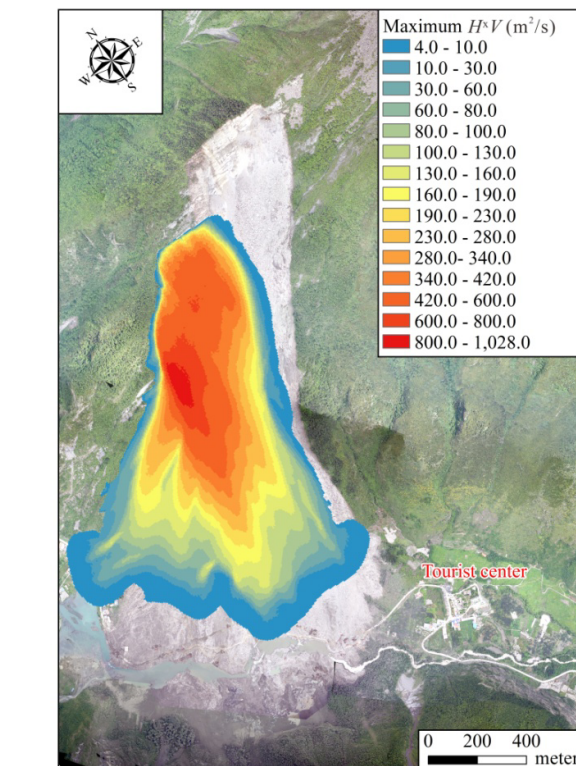


Figure 6 The dynamic characteristics and predicted danger area of the unstable block. (a) The initial thickness of potential failure blocks estimated by field investigation; (b) The maximum thickness of the rock mass in sliding process. (c) The maximum flow height (H) \times velocity (V) of the rock mass in sliding process.

Acknowledgments

Field helps from the armed police traffic team are highly appreciated. Financial support from National Nature Science Foundation of China (Grant No. 41572303, 41520104002), Chinese Academy of Sciences “Light of West China” Program and Youth Innovation Promotion Association, is acknowledged.

References

- Banton J, Villard P, Jongmans D, Scavia C (2009) Two-dimensional discrete element models of debris avalanches: Parameterization and the reproducibility of experimental results. *Journal of Geophysical Research: Earth Surface* 114(F4). <https://doi.org/10.1029/2008JF001161>
- Beyabanki SAR, Bagtzoglou AC, Liu L (2016) Applying disk-based discontinuous deformation analysis (DDA) to simulate Donghekou landslide triggered by the Wenchuan earthquake. *Geomechanics and Geoengineering* 11(3): 177-188. <https://doi.org/10.1080/17486025.2015.1082647>

- Burgh LVD, Stoffel M, Bigler C (2012) Analysis and modeling of tree succession on a recent rockslide deposit. *Plant Ecology* 213(1): 35-46. <https://doi.org/10.1007/s11258-011-0004-2>
- Chen HX, Zhang S, Peng M, et al. (2016) A physically-based multi-hazard risk assessment platform for regional rainfall-induced slope failures and debris flows. *Engineering Geology* 203: 15-29. <https://doi.org/10.1016/j.enggeo.2015.12.009>
- Coe JA, Baum RL, Allstadt KE, et al. (2016) Rock-avalanche dynamics revealed by large-scale field mapping and seismic signals at a highly mobile avalanche in the West Salt Creek valley, western Colorado. *Geosphere* 12(2): 607-631. <https://doi.org/10.1130/GES01265.1>
- Delaney KB, Evans SG (2015) The 2000 Yigong landslide (Tibetan Plateau), rockslide-dammed lake and outburst flood: Review, remote sensing analysis, and process modelling. *Geomorphology* 246: 377-393. <https://doi.org/10.1016/j.geomorph.2015.06.020>
- Guthrie RH, Evans SG, Catane SG, et al. (2009) The 17 February 2006 rockslide-debris avalanche at Guinsaugon Philippines: a synthesis. *Bulletin of engineering geology and the environment* 68: 201-213. <https://doi.org/10.1007/s10064-009-0205-2>
- Fan JR, Zhang XY, Su FH, et al. (2017) Geometrical feature analysis and disaster assessment of the Xinmo landslide based on remote sensing data. *Journal of Mountain Science* 14(9). <https://doi.org/10.1007/s11629-017-4633-3>
- He SM, Ouyang CJ, Liu W, et al. (2016) Coupled model of two-phase debris flow, sediment transport and morphological evolution. *Acta Geologica Sinica (English Edition)* 90(6): 2206-2215. <https://doi.org/10.1111/1755-6724.13031>
- Hungr O, Evans SG (2004) Entrainment of debris in rock avalanches: An analysis of a long run-out mechanism. *Geological Society of America Bulletin* 116(9-10): 1240-1252. <https://doi.org/10.1130/B25362.1>
- Iverson RM, George DL (2015) Modelling landslide liquefaction, mobility bifurcation and the dynamics of the 2014 Oso disaster. *Geotechnique* 66(3): 175-187. <https://dx.doi.org/10.1680/jgeot.15.LM.004>
- Iverson RM, Ouyang CJ (2015) Entrainment of bed material by Earth - surface mass flows: Review and reformulation of depth - integrated theory. *Reviews of Geophysics* 53(1): 27-58. <https://doi.org/10.1002/2013RG000447>
- Liang Q (2010) Flood simulation using a well-balanced shallow flow model. *Journal of hydraulic engineering* 136(9): 669-675. [https://doi.org/10.1016/\(ASCE\)HY.1943-7900.0000219](https://doi.org/10.1016/(ASCE)HY.1943-7900.0000219)
- Liu W, He SM, Ouyang CJ (2016) Dynamic process simulation with a savage-hutter type model for the intrusion of landslide into river. *Journal of Mountain Science* 13(7): 1265-1274. <http://doi.org/10.1007/s11629-015-3439-4>
- Ouyang CJ, He SM, Xu Q, et al. (2013) A MacCormack-TVD finite difference method to simulate the mass flow in mountainous terrain with variable computational domain. *Computers and Geosciences* 52: 1-10. <https://doi.org/10.1016/j.cageo.2012.08.024>
- Ouyang CJ, He SM, Tang C (2015a) Numerical analysis of dynamics of debris flow over erodible beds in Wenchuan earthquake-induced area. *Engineering Geology* 194: 62-72. <https://doi.org/10.1016/j.enggeo.2014.07.012>
- Ouyang CJ, He SM, Xu Q (2015b) MacCormack-TVD finite difference solution for dam break hydraulics over erodible sediment beds. *Journal of Hydraulic Engineering* 141(5): 06014026. [https://doi.org/10.1061/\(ASCE\)HY.1943-7900.0000986](https://doi.org/10.1061/(ASCE)HY.1943-7900.0000986)
- Ouyang C, Zhou K, Xu Q, et al. (2017) Dynamic analysis and numerical modeling of the 2015 catastrophic landslide of the construction waste landfill at guangming, shenzhen, china. *Landslides* 14(2): 705-718. <https://doi.org/10.1007/s10346-016-0764-9>
- Savage SB, Hutter K (1989) The motion of a finite mass of granular material down a rough incline. *Journal of Fluid Mechanics* 199: 177-215. <https://doi.org/10.1017/S0022112089000340>
- Shi C, Li DJ, Chen KH, et al. (2016) Failure mechanism and stability analysis of the zhenggang landslide in Yunnan province of China using 3d particle flow code simulation. *Journal of Mountain Science* 13(5): 891-905. <https://doi.org/10.1007/s11629-014-3399-0>
- Su LJ, Hu KH, Zhang WF, et al. (2017) Characteristics and triggering mechanism of Xinmo landslide on 24 June 2017 in Sichuan, China. *Journal of Mountain Science* 14(9). <https://doi.org/10.1007/s11629-017-4609-3>
- Wang YF, Dong JJ, Cheng QG (2017) Velocity - dependent frictional weakening of large rock avalanche basal facies: Implications for rock avalanche hypermobility? *Journal of Geophysical Research: Solid Earth* 122(3): 1648-1676.
- Wu JH, Chen JH, Lu CW (2013) Investigation of the hsien-du-shan rock avalanche caused by typhoon morakot in 2009 at kaohsiung county, taiwan. *International Journal of Rock Mechanics & Mining Sciences* 60(2): 148-159. <https://doi.org/10.1016/j.ijrmms.2012.12.033>
- Xing A, Wang G, Li B, et al. (2014) Long-runout mechanism and landsliding behavior of large catastrophic. *Canadian Geotechnical Journal* 52(7): 971-981. <https://doi.org/10.1139/cgj-2014-0122>
- Xu Q, Fan X, Huang R, et al. (2010) A catastrophic rockslide-debris flow in Wulong, Chongqing, China in 2009: background, characterization, and causes. *Landslides* 7: 75-87. <https://doi.org/10.1007/s10346-009-0179-y>
- Zhang H, Liu SG, Wang W, et al. (2016) A new DDA model for kinematic analyses of rockslides on complex 3-d terrain. *Bulletin of Engineering Geology & the Environment* 1-17. <https://doi.org/10.1007/s10064-016-0971-6>
- Zhou JW, Huang KX, Shi C, et al. (2015). Discrete element modeling of the mass movement and loose material supplying the gully process of a debris avalanche in the Bayi Gully, Southwest China. *Journal of Asian Earth Sciences* 99: 95-111. <https://doi.org/10.1016/j.jseaes.2014.12.008>